INVITED PAPER   *Special Section on Electronic Displays*

Millimeter-Wave Single-Pixel Imaging Using Electrically-Switchable Liquid-Crystal Mask

Michinori HONMA[†a)]**,** *Member***, Takashi SASE**[†]**, Ryota ITO**[†]**,** *Nonmembers***,** *and* **Toshiaki NOSE**[†]**,** *Member*

SUMMARY   In this study, we have proposed a millimeter-wave (MMW) single-pixel imaging (SPI) system with a liquid-crystal (LC) mask cell. The LC cell functions as an electrically switchable mask based on the change in absorption properties, which depend on the orientation of the LC. We investigated the influence of noise on the measured and estimated data (reconstructed image). The proposed system exhibited moderate robustness against random noise (that were added) compared to raster scan-based and Hadamard matrix-based SPI systems. Finally, the results of some demonstrative experiments were introduced to ensure the applicability of the constructed MMW-SPI system, and steps for improving the reconstructed image quality were discussed.
key words: *liquid crystal, millimeter-wave, millimeter-wave imaging, single pixel imaging, computational imaging*

1. Introduction

Millimeter-wave (MMW) imaging technology is used in various practical applications, such as nondestructive inspections [1], material analysis [2], security surveillance [3], disaster rescue operations [4], and remote sensing [5]. MMW penetrates into ordinary dielectrics, including plastics, papers, and clothes [6], and conductors such as metals greatly reflect MMW. Because the squared penetration length is inversely proportional to the MMW frequency, the wave deeply invades dielectric objects compared to visible light and THz waves. Hence, this property of permeability is exploited in various nondestructive inspection systems; for example, the detection of metal pieces concealed in closed envelopes and drywalls [7], inspection of cracks generated inside concrete walls [1], [8], [9], quality checks of cork [10], sorting of broken cookies [9], kerogen investigations [11], and detection of photo-excited free carriers in Si wafers [12]. Furthermore, several organic dielectrics exhibit characteristic absorption spectra in the MMW region [10], [13], which enables material identification. It is well known that water is an effective MMW absorber. Hence, MMW is useful for detecting the moisture in grains [14], fruits [15], wood [16], and pharmaceuticals [17]. In addition, MMW is transparent to smoke and flames [4], [18], [19], that is, MMW inspections can determine lives during disaster rescue operations.

MMW is classified as a non-ionizing radiation and therefore, do not possess hazards to human health. This is an advantage over ionizing radiations such as X-rays. A well-known example of the security surveillance system using MMW is the airport security gate that finds objects concealed behind clothes [3], [20].

In general, the MMW frequency ranges from 30 – 300 GHz, corresponding to a wavelength range of 1 – 10 mm. In this frequency range, the MMW is absorbed by water and oxygen present in the atmosphere. However, atmospheric windows for less absorption exist at 35, 94, 140, and 220 GHz [5], further enabling atmospheric remote sensing applications.

A classical MMW imaging method is the raster scan [1], [21], [22], which uses an MMW detector in which a certain position in a measuring plane corresponds to one measured data in a one-to-one relationship. An arrayed antenna combined with a dielectric lens [23], [24] can reduce the data acquisition time. This measurement system is equivalent to conventional imaging optical systems. The image resolution is governed by the Nyquist limit, which is equal to half the free-space wavelength.

In addition to this classical method, a different type of imaging technology (lensless imaging) [25], [26] has gained significant attention. In classical imaging optics, MMW rays emitted from a certain point in space converge into an imaging plane where a detector is placed. However, in the absence of imaging optics, the detector collects several MMW rays emitted from multiple positions on the object surface. In this type of imaging system, images are reconstructed by solving an inverse problem using one-dimensional (1D) data, which is obtained via spatially or temporarily separated independent measurements. Computer-assisted image reconstruction is referred as computational imaging (CI). Recent progress in consumer hardware has overcome technical obstacles in CI developments.

A holographic technique [27] is a feasible method to reconstruct images from 1D measured data. However, not only the amplitude, but also the phase information are generally required for reconstructing images. Unlike holographic methods, only time-series amplitude (intensity) data acquired with a detector are necessary in single-pixel imaging (SPI) systems [28]. The simple architecture composed of an emitter, a switchable mask, and a detector is an attractive aspect of SPI systems. This method can be adopted in all frequency regions, from X-rays to microwaves and even acoustic waves. An antenna array is no longer required for SPI systems. Instead of an arrayed antenna, time-series data
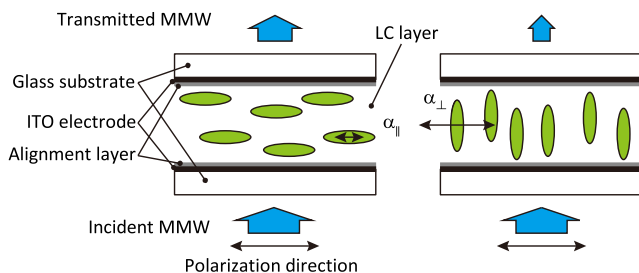
must be acquired by changing the mask pattern. The choice of mask pattern influences the reconstructed image quality. Therefore, a set of switchable masks must be appropriately selected depending on the practical demands for resolution, signal-to-noise ratio (SNR), and measurement time.

Digital mirror devices (DMDs) and liquid crystal (LC) spatial light modulators (SLMs) can be used as electrically switchable amplitude masks [28], [29]. Ordinary DMDs and LC-SLMs exhibit high light-beam controllability for visible light. However, these devices must be customized based on the physical characteristics of the MMW. One simple architecture of the MMW-controlling device is a passive matrix LC cell that is composed only of substrates, electrodes, alignment layers, and an LC layer. In ordinary passive matrix LC devices, steep transmittance-voltage characteristics are required to avoid crosstalk. Furthermore, the number of electrodes was limited when the device was operated under ordinary passive matrix addressing. Fortunately, crosstalk is no longer a serious issue in SPI because multiple pixels are in the on-state in an LC switchable mask. However, it is important to clarify the influence of masks on the reconstructed image quality. In this study, we have introduced an MMW-SPI system that uses a planar alignment LC cell with a matrix electrode structure [30] that functions as an electrically switchable amplitude mask. We have also discussed the influence of a set of mask patterns on mean square errors (MSEs) of the reconstructed images. Finally, we have presented the results of the demonstrative experiment, in which a small metal piece concealed with an opaque paper sheet is appropriately detected.

2. LC Mask Cell and Driving Circuit

The large optical anisotropies of nematic LCs in the MMW region (birefringence and dichroism) are attractive for the realization of various electrically controllable LC devices [31]–[33]. The usual planar alignment LC cell can vary the MMW transmittance with respect to applied voltage because the absorption amount depends on the LC orientation direction. It should be noted that the intensity of the output MMW could be modulated without using a polarizer. Furthermore, a dichroic dye, which is usually used in LC optical devices, was not required in this study.

Figure 1 depicts the structure of the fabricated LC cell that can modulate the incident MMW. The LC cell used in this study is similar to a conventional planar alignment LC cell, except for the relatively large sheet resistance (>100 Ω/sq) of indium-tin-oxide (ITO) layers and a thick LC layer (130 μm). A large sheet resistance was preferred for increasing the MMW transmittance, which was estimated to be a few percent. The thick LC layer led to a high contrast ratio for the MMW switching. We used a commercially available ITO/glass substrates (0.4 mm thickness, Kuramoto). At first, they were ultrasonically precleared, and thereafter, the polyimide (SE2170, Nissan Chemical Industries) was spin-coated on the substrates. Subsequently, they were baked at 200°C for 1 h. After an empty cell was constructed by combining two substrates, 5CB (4-cyano-4′-pentylbiphenyl) was injected into the glass gap.

A difficulty while developing LC MMW devices is the conflict that arises between good MMW transparency and high electrical conductivity. The use of conductive polymers, such as poly(3,4-ethylenedioxythiophene), is a better alternative for realizing practical LC MMW-controlling devices [34]. However, the high chemical, electrical, photo, and temporal stabilities of ITO are useful for practical applications. Some researchers are concerned about the high MMW reflectance of ITO. However, low throughput cannot be a priority issue in MMW sensing applications. The required priority of our MMW-SPI system is different from that of energy-transferring devices, including beam-scanning antennas and beam formers. We adopted a lock-in detection system to secure accurate measurements of MMW signals during MMW-SPI operations.

When no voltage was applied across the LC cell, the MMW transmittance was governed by the absorption coefficient in the LC orientation direction ($\alpha_{\parallel}$). The LC molecules tend to tilt up with respect to the substrate plane as the applied voltage increases. Finally, they became perpendicular to the substrate plane at a sufficiently high applied voltage. In this situation, the absorption coefficient in the direction perpendicular to the LC orientation ($\alpha_{\perp}$) becomes dominant. Here, it should be noted that $\alpha_{\perp}$ is greater than $\alpha_{\parallel}$ in the MMW region. Consequently, the MMW transmittance decreased with increasing applied voltage when the polarization direction was parallel to the LC orientation. In contrast, the MMW transmittance remained constant when the polarization direction was perpendicular. It should be noted that perfect homeotropic orientation is unachievable in thick LC cells. Hence, the contrast ratio during switching is smaller than expected, leading to a decrease in the SNR.

Figure 2 depicts the constructed electric circuit that changes the spatial distribution pattern of the transmitted MMW. A matrix electrode structure was formed by crossing the stripe electrodes. All row and column electrodes were grounded or biased (sinusoidal wave, 1 kHz, 30 V$_{rms}$) separately. As mentioned in the previous section, multiple pixels are in the on-state when one row and column electrodes are simultaneously addressed. Specifically, when the r1 and c1 electrodes are selected at the top-left pixel as depicted in Fig. 2, where the two electrodes intersect, no electric field is
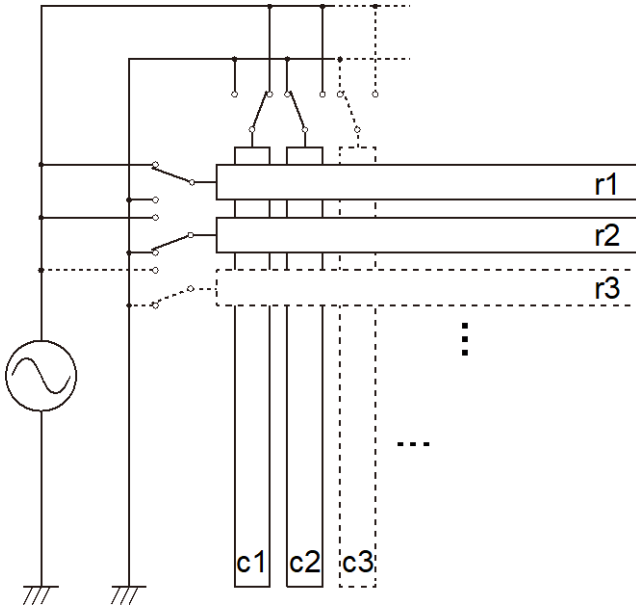

Fig. 1 Structure of an LC cell that can modulate the intensity of incident MMW based on an anisotropic absorption coefficient that can be varied depending on the direction of LC orientation.

Fig. 2 Electric circuit for driving the LC mask cell that is constructed by orthogonally combining eight rows and eight columns of electrodes. All row and column electrodes are either grounded or biased (sinusoidal wave, 1 kHz, 30 V$_{rms}$). During operation, a pair of one row and column electrodes is addressed and others are grounded.

Fig. 3 Construction of MMW-SPI system with an LC mask cell. Specimens are inserted between a transmitting Horn antenna and the LC cell. The polarization direction of MMW coincides with the orientation direction of the LC cell. All MMW bundle transmitted through the LC cell is collected using a receiving horn antenna.

generated in the LC layer because the electric potentials at the two electrodes are the same. Hence, the pixel remains off. In contrast, the uppermost and leftmost pixels turn on, except for the top-left pixel. The voltage across the LC layer, V_{LC} is expressed as an exclusive OR operation of the electric potentials at the row and column electrodes (V_r and V_c) as follows:
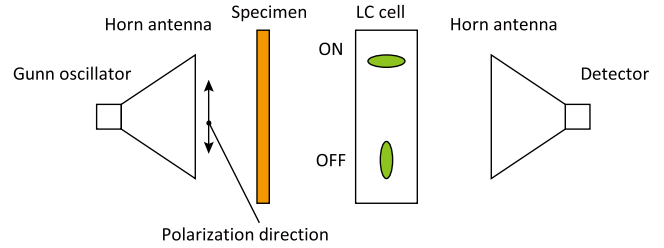
$$V_{LC} = V_r \oplus V_c \tag{1}$$

Namely, $V_{LC} = 0$ when $V_r = V_c$, while $V_{LC} = 30$ V$_{rms}$ when $V_r \neq V_c$.

3. MMW-SPI System

The constructed LC MMW-SPI system has a simple architecture, as depicted in Fig. 3. The system is composed of three devices: a Gunn oscillator (70 GHz), a Schottky diode detector, and an LC mask cell. The MMW emitted from the oscillator was linearly polarized and was expanded using a horn antenna. The emitted MMW was first incident on a specimen, and thereafter, propagated toward the LC mask cell. The spatial distribution profile of the MMW intensity was modulated depending on the mask pattern produced by the LC cell. Finally, the second horn antenna collected the transmitted MMW and the MMW intensity was integrated over the aperture plane of the antenna.

The SPI measurement in the constructed system was completed in 10 min or longer. Random noise of the output voltage was carefully eliminated using a lock-in detection scheme. A personal computer acquired data every second, and then several (5–10) accumulated data points were

averaged to further suppress the noise. This averaging was repeated 64 times (the number of pixels) by changing the mask pattern. One simple method to reduce the measurement time is to reduce the response time of the LC device. Thinner LC devices can reduce the response time. However, a decrease in the transmittance contrast ratio during switching is a possible tradeoff.

An iterative measurement of the MMW intensity was performed by varying the mask pattern. Let us assume that **y** is a 1D vector that is composed of all measured MMW intensities y_i (i is an integer), and **x** is also a 1D vector that is constructed by rearranging intensity data x_i at all positions on the specimen plane. Here, we assume that a linear relation, $\mathbf{y} = \mathbf{Ax}$, is satisfied in the system, where **A** is the measurement matrix. In general, diffraction and interference phenomena inevitably affected the MMW intensity measurements as the MMW propagated in free space. In this situation, the MMW propagation cannot be discussed based on geometric optics, which means that the simple linear relation, $\mathbf{y} = \mathbf{Ax}$, might not be a reasonable assumption. To avoid such an undesirable situation, we placed the LC mask cell immediately behind the specimen plane. Hence, the measured MMW intensity can be expressed as the sum of the MMW intensities for all pixels; this fact secures the relation, $\mathbf{y} = \mathbf{Ax}$. When the number of measurements, M and pixels, N are equal ($M = N$), the MMW images are reconstructed by solving the following equation: $\mathbf{x} = \mathbf{A}^{-1}\mathbf{y}$. However, when M is not equal to N ($M \neq N$), the executing calculation must be $\mathbf{x} = \mathbf{A}^{\dagger}\mathbf{y}$, where $\mathbf{A}^{\dagger}$ is the pseudo-inverse. Here, we set both M and N as 64.

Figure 4 depicts the creation of measurement matrix **A** from the mask pattern. At first, the mask patterns of all the measurements were prepared, as depicted in Fig. 4 (step 1). In Fig. 4, the white and black pixels denote the on- and off-states, respectively, and i is the number of measurements. The mask pattern was shredded into eight rows of data, which were concatenated to form one row of data (step 2). Finally, the produced rows of data were combined into two-dimensional matrix data (step 3). The lowermost picture is the measurement matrix **A** that was used during the image reconstruction process.
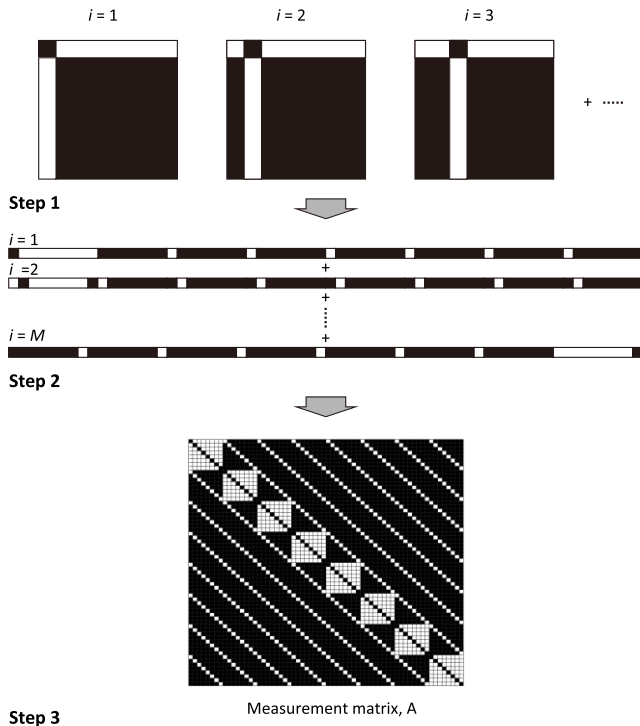
Fig. 4 Production procedure of the measurement matrix **A** used in the MMW-SPI system. White and black pixels denote on- and off-state pixels, respectively, and i is the number of measurements.

Fig. 5 Relationship between the MSE and number of examination in the case when the added noise has (a) a correlation or (b) no correlation with the MMW intensity.

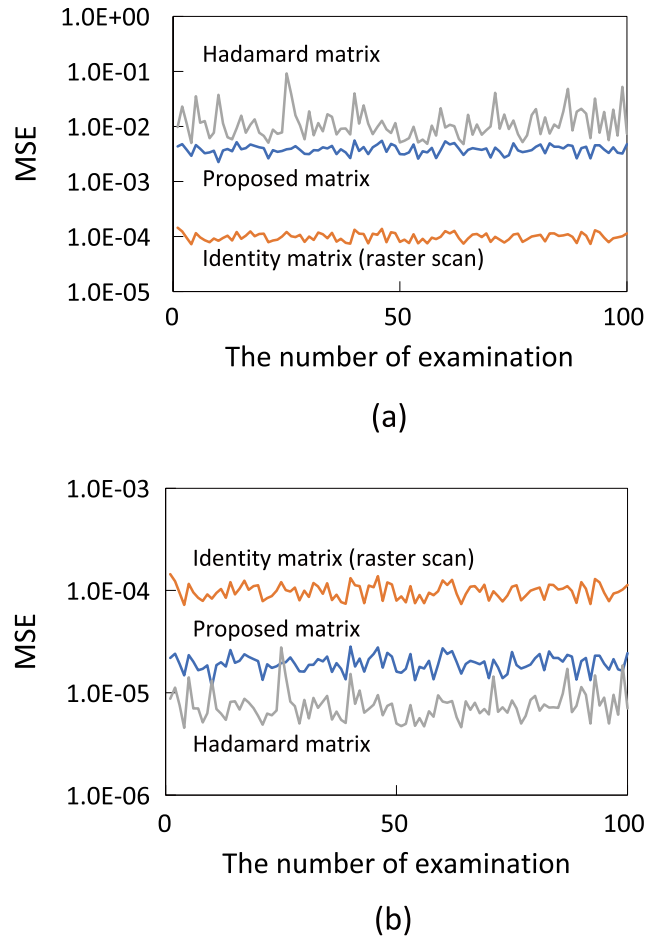## 4. Influence of Random Noise on Estimated Data

It is important to discuss the effect of a given noise on the quality of the reconstructed image. Here, we added two types of random noise that are present in the measurement system and the detector. Generally, various uncertain fluctuations, such as the mechanical movement of components, drift of driving voltage, and temperature swing of material parameters, arise and mix independently, further causing random noise. The noise level is assumed to be proportional to the input MMW intensity. In other words, the generated random noise can be correlated with the MMW intensity. Consequently, the measured data $\mathbf{y}_c$ can be defined using the signal and fluctuating components ($\mathbf{y}_s$ and $\mathbf{y}_f$, respectively) as follows:

$$\mathbf{y}_c = \mathbf{y}_s + \mathbf{y}_s \circ \mathbf{y}_f. \tag{2}$$

The product $\mathbf{y}_s \circ \mathbf{y}_f$ expresses a noise component, where the symbol "∘" denotes the Hadamard product.

Overall, the undesirable noise generated in the measurement system can be eliminated or reduced by employing a sophisticated system design and a careful preparation procedure. However, the thermal noise of a detector, such as the shot noise, is unavoidable. In this case, the noise level had no correlation with the MMW intensity, which implies that the measured data $\mathbf{y}_u$ can be simply expressed as the sum of $\mathbf{y}_s$ and $\mathbf{y}_f$.

$$\mathbf{y}_u = \mathbf{y}_s + \mathbf{y}_f. \tag{3}$$

The influences of both noises on the estimated data are summarized. Figure 5 (a) and 5 (b) depict the mean square errors (MSEs) with and without correlation, respectively. MSE is defined as:

$$\text{MSE} = \frac{1}{N} \sum_{j=1}^{N} \left(\hat{x}_j - x_j \right)^2, \tag{4}$$

swhere x_j is the true value, $\hat{x}_j$ is the estimated data when $\mathbf{y}_f$ is added, and j is the pixel number. MSE can be replaced by variance σ^2, where σ represents the standard deviation. We set $N = 64$ and $x_j = 1$ for the MSE examination. The average and standard deviation of $\mathbf{y}_f$ were set as 0 and 0.01, respectively, and the $\mathbf{y}_f$ values were random. The examination was repeated 100 times. Two typical measurement matrices were chosen for comparison: the Hadamard and identity matrices. The Hadamard matrix is considered the best candidate for achieving optimal performance in SPI systems. An identity matrix is used in the case of raster scan measurement, in which the intensity of the MMW transmitted through only one pixel is measured separately by scanning the pixel.

From Fig. 5 (a), it can be seen that the identity matrix

yields a small MSE when $\mathbf{y}_f$ correlates with $\mathbf{y}_s$. The estimated data and measured data are equal, that is, $\mathbf{x} = \mathbf{y}$. Consequently, the fluctuations of $\mathbf{x}$ and $\mathbf{y}$ have the same standard deviations of 0.01; that is, the variance (MSE) is 10^{-4}. When the Hadamard matrix is used, the measured MMW intensity increases because nearly half of the pixels are in on-state. This implies that the noise of the measured data $\mathbf{y}_s \circ \mathbf{y}_f$ increases with an increase in the signal component $\mathbf{y}_s$. In our LC mask, 14 pixels were in the on-state. Hence, the evaluated MSE is larger than that of the identity matrix and smaller than that of the Hadamard matrix.

When $\mathbf{y}_f$ has no correlation with $\mathbf{y}_s$, the opposite tendency was observed in Fig. 5 (b); that is, the MSE of the Hadamard matrix exhibited the lowest level and that of the identity matrix indicated the highest level. Therefore, the Hadamard matrix is occasionally chosen in practical SPI systems. As mentioned previously, the thermal fluctuation of a detector is unavoidable and has no correlation with the measured MMW intensity. Therefore, in the raster scan, the SNR of the measurement would be worse, while SNR is increased when the Hadamard matrix and our measurement matrix are used. This type of merit is termed Fellgett's advantage or multiplex advantage. From Figs. 5 (a) and 5 (b), we can see that our measurement matrix has moderate robustness for the two types of noise with and without correlation.

5. MMW-SPI

In this section, we have introduced the results of the demonstrative experiment obtained using the MMW-SPI system constructed using the LC mask cell. A small copper sheet was examined as a specimen. The incident MMW was strongly reflected by the copper sheet because of its high electrical conductivity. Therefore, the presence of the copper sheet is indicated as the dark area in the image. Figure 6 depicts reconstructed images as the copper sheet rotated from $-135° - 90°$. The dotted squares denote the positions of the specimen. The reconstructed image area was 16×16 mm, and the number of pixels was 64 (eight rows and columns). The reconstructed image data were normalized such that the maximum value was unity. In the experiment, the copper sheet was fully covered with opaque paper so that the sheet was invisible to the naked eye. It is evident from Fig. 6 that a dark region was recognized, although the copper sheet was completely invisible. Furthermore, the dark region rotated according to the rotation of the specimen. We can conclude that the constructed MMW-SPI system using an LC mask cell can detect the position and direction of concealed metal objects.

As depicted in Fig. 6, the blur in the constructed image is an issue that needs to be solved. The SNR of the measured data must be improved to obtain clearer images. To achieve this, the contrast ratio of the MMW intensity should be increased while switching the LC cell. The absorption coefficients of the LC material we used (5CB) are $(\alpha_\parallel =) 0.018$ and $(\alpha_\perp =) 0.030$ mm^{-1}. Accordingly, the
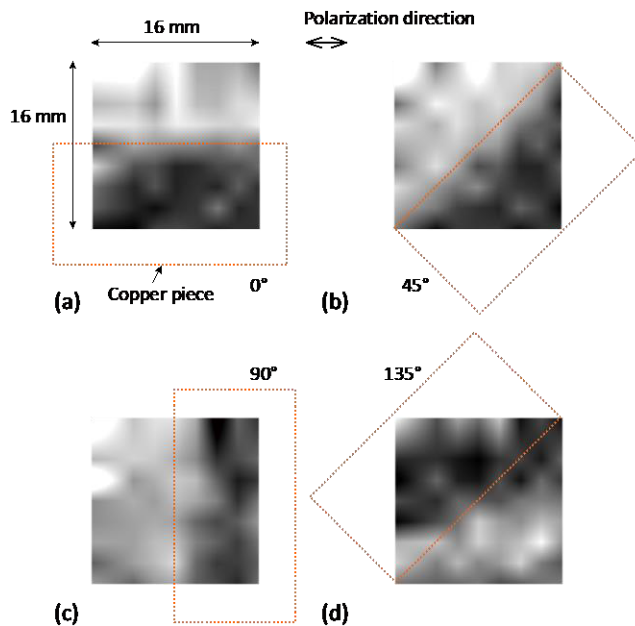
Fig. 6 Reconstructed images obtained using the proposed MMW-SPI system with an LC mask cell. A copper sheet placed behind an opaque paper sheet was used as a test sample. The angle of the sample was set at (a) 0°, (b) 45°, (c) 90°, and (d) −135°. The dotted rectangle indicates the position and direction of the examined copper sheet.

transmittances of the LC layer (130 μm thick) were evaluated to be 99.77 and 99.61% for the parallel and perpendicular directions, respectively. Therefore, only 0.16% of the incident MMW intensity was reduced while switching. It was difficult to find an MMW signal buried in noisy data. In the demonstrative experiment, we extracted the signal components using a lock-in detection technique. Based on our preliminary examination, we estimated that the transmittance of our device was lower than 10%. The change in the output voltage during switching was less than 1%, which was comparable to the theoretical estimation (0.16%). Further improvement in the contrast ratio is helpful for increasing the SNR of the measured data.

Other improvements should be performed to optimize the size and arrangement (alignment) of each component used in the system. These parameters influence the quality of the reconstructed image. In particular, the relationship between the MMW wavelength and pixel size is crucial because a small pixel easily diffracts an incident MMW. A significant amount of diffraction leads to a break in the linear model assumption $\mathbf{y} = \mathbf{Ax}$.

In this study, the distance between the specimen and the mask was set as zero to eliminate undesirable diffracted MMW components. Furthermore, the incident MMW become less sensitive to the minute mask pattern when the pixel size is less than the wavelength. This wavelength region is referred to as the effective medium approximation (EMA) region. In the EMA region, the pixel size is no longer a critical parameter governing the resolution. Instead, the resolution is directly dependent on the effective refractive index and absorption coefficient of the mask.

In addition, it is important that the influence of noise on reconstructed images can be reduced depending on the choice of measurement matrix **A**. In this study, we used a mask pattern created by simultaneously addressing only one row and one column of electrodes. However, the selection of multiple rows and columns of electrodes may result in better performance of the system.

6. Conclusions

In this study, we have proposed an MMW-SPI system incorporated with an LC mask cell. The influence of noise (fluctuation), which was added to measured data, on estimated data (reconstructed image), was investigated. It was found that the proposed system exhibits moderate robustness against random noise compared to the raster scan-based and Hadarmard matrix mask-based SPI systems. Furthermore, a demonstrative experiment proved the applicability of the constructed MMW-SPI system, that is, we detected the position and direction of a metal piece placed behind an opaque paper sheet. The proposed system will be helpful for invisible or concealed object search applications.

References

[1] S. Kharkovsky and R. Zoughi, "Microwave and millimeter wave nondestructive testing and evaluation-Overview and recent advances," IEEE Instrum. Meas. Mag., vol.10, no.2, pp.26–38, 2007.

[2] D. Bourreau, A. Péden, and S. Le Maguer, "A quasi-optical free-space measurement setup without time-domain gating for material characterization in the W-band," IEEE Trans. Instrum. Meas., vol.55, no.6, pp.2022–2028, 2006.

[3] R. Appleby and R.N. Anderton, "Millimeter-wave and submillimeter-wave imaging for security and surveillance," Proc. IEEE, vol.95, no.8, pp.1683–1690, 2007.

[4] C. Li and L. Chang, "Study on the Applicability of Passive Millimeter Wave Imaging Technology in Real Fire," IOP Conference Series: Materials Science and Engineering, vol.612, no.5, p.052052, 2019.

[5] R. Appleby, "Passive millimetre–wave imaging and how it differs from terahertz imaging," Philos. Trans. Royal Soc. A: Mathematical, Physical and Engineering Sciences, vol.362, no.1815, pp.379–393, 2004.

[6] J.E. Bjarnason, T.L.J. Chan, A.W.M. Lee, M.A. Celis, and E.R. Brown, "Millimeter-wave, terahertz, and mid-infrared transmissionthrough common clothing," Appl. Phys. Lett., vol.85, no.4, pp.519–521, 2004.

[7] F. Zhang, C. Wu, B. Wang, and K.J.R. Liu, "mmEye: Super-resolution millimeter wave imaging," IEEE Internet Things J., vol.8, no.8, pp.6995–7008, 2020.

[8] J. Nadakuduti, G. Chen, and R. Zoughi, "Semiempirical electromagnetic modeling of crack detection and sizing in cement-based materials using near-field microwave methods," IEEE Trans. Instrum. Meas., vol.55, no.2, pp.588–597, 2006.

[9] S. Oka, H. Togo, N. Kukutsu, and T. Nagatsuma, "Latest trends in millimeter-wave imaging technology," Prog. Electromagn. Res. Lett., vol.1, pp.197–204, 2008.

[10] Y.L. Hor, J.F. Federici, and R.L. Wample, "Nondestructive evaluation of cork enclosures using terahertz/millimeter wave spectroscopy and imaging," Appl. Opt., vol.47, no.1, pp.72–78, 2008.

[11] J.A. Scales and M. Batzle, "Millimeter wave analysis of the dielectric properties of oil shales," Appl. Phys. Lett., vol.89, no.2, p.024102, 2006.

[12] T. Nozokido, J. Bae, and K. Mizuno, "Scanning near-field millimeter-wave microscopy using a metal slit as a scanning probe," IEEE Trans. Microw. Theory Techn., vol.49, no.3, pp.491–499, 2001.

[13] J.A. Scales and M. Batzle, "Millimeter wave spectroscopy of rocks and fluids," Appl. Phys. Lett., vol.88, no.6, p.062906, 2006.

[14] K.Y. You, H.K. Mun, L.L. You, J. Salleh, and Z. Abbas, "A small and slim coaxial probe for single rice grain moisture sensing," Sensors, vol.13, no.3, pp.3652–3663, 2013.

[15] F. Zidane, J. Lanteri, J. Marot, L. Brochier, N. Joachimowicz, H. Roussel, and C. Migliaccio, "Nondestructive control of fruit quality via millimeter waves and classification techniques: Investigations in the automated health monitoring of fruits," IEEE Antennas Propag. Mag., vol.62, no.5, pp.43–54, 2020.

[16] S. Tanaka, Y. Fujiwara, Y. Fujii, S. Okumura, H. Togo, N. Kukutsu, and S. Mochizuki, "Dielectric anisotropy of oven-and air-dried wood evaluated using a free space millimeter wave," J. Wood Sci., vol.59, no.5, pp.367–374, 2013.

[17] L. Gradinarsky, H. Brage, B. Lagerholm, I.N. Björn, and S. Folestad, "In situ monitoring and control of moisture content in pharmaceutical powder processes using an open-ended coaxial probe," Meas. Sci. Technol., vol.17, no.7, p.1847, 2006.

[18] M. Sakai and Y. Aoki, "Human and object detection in smoke-filled space using millimeter-wave radar based measurement system," 18th International Conference on Pattern Recognition (ICPR'06) IEEE, Hong Kong, China, vol.3, p.750, Aug. 2006.

[19] J.W. Starr and B.Y. Lattimer, "Evaluation of navigation sensors in fire smoke environments," Fire Technol., vol.50, no.6, pp.1459–1481, 2014.

[20] Z. Wang, T. Chang, and H.-L. Cui, "Review of active millimeter wave imaging techniques for personnel security screening," IEEE Access, vol.7, pp.148336–148350, 2019.

[21] M.D. Weiss, B. Zadler, S. Schafer, and J. Scales, "Near field millimeter wave microscopy with conical Teflon probes," J. Appl. Phys., vol.106, no.4, p.044912, 2009.

[22] W.-G. Kim, N.-W. Moon, M.K. Singh, H.-K. Kim, and Y.-H. Kim, "Characteristic analysis of aspheric quasi-optical lens antenna in millimeter-wave radiometer imaging system," Appl. Opt., vol.52, no.6, pp.1122–1131, 2013.

[23] H. Sato, K. Sawaya, K. Mizuno, J. Uemura, M. Takeda, J. Takahashi, and J. Nakada, "Development of 77 GHz millimeter wave passive imaging camera," Proc. IEEE Sensors, Christchurch, New Zealand, pp.1632–1635, Oct. 2009.

[24] K. Yang, J. Wang, L. Zhao, Z. Liu, and T. Zhang, "Millimeter-wave imaging with slab focusing lens made of electromagnetic-induction materials," Opt. Express, vol.24, no.1, pp.566–572, 2016.

[25] L. Spinoulas, J. Qi, A.K. Katsaggelos, T.W. Elmer, N. Gopalsami, and A.C. Raptis, "Optimized compressive sampling for passive millimeter-wave imaging," Appl. Opt., vol.51, no.26, pp.6335–6342, 2012.

[26] Q. Cheng, A. Alomainy, and Y. Hao, "Compressive millimeter-wave phased array imaging," IEEE Access, vol.4, pp.9580–9588, 2016.

[27] R.J. Mahon, J.A. Murphy, and W. Lanigan, "Digital holography at millimetre wavelengths," Opt. Commun., vol.260, no.2, pp.469–473, 2006.

[28] M.F. Duarte, M.A. Davenport, D. Takhar, J.N. Laska, T. Sun, K.F. Kelly, and R.G. Baraniuk, "Single-pixel imaging via compressive sampling," IEEE Signal Process. Mag., vol.25, no.2, pp.83–91, 2008.

[29] G. Huang, H. Jiang, K. Matthews, and P. Wilford, "Lensless imaging by compressive sensing," 2013 IEEE International Conference on Image Processing, Melbourne, VIC, Australia, pp.2101–2105, Sept. 2013.

[30] T. Nozokido, S. Maede, N. Miyasaka, H. Okada, T. Nose, and T. Murai, "A millimeter-wave quasi-optical grid phase shifter using liquid crystal," IEICE Electron. Express, vol.7, no.2, pp.67–72, 2010.

[31] T. Nose, M. Honma, T. Nozokido, and K. Mizuno, "Determination of the insertion loss and refractive index anisotropy in nematic liquid

crystal materials using a V-band waveguide transmission cell," Mol. Cryst. Liq. Cryst., vol.409, no.1, pp.199–207, 2004.

[32] T. Nose, M. Honma, T. Nozokido, and K. Mizuno, "Simple method for the determination of refractive indices and loss parameters for liquid-crystal materials in the millimeter-wave region," Appl. Opt., vol.44, no.7, pp.1150–1155, 2005.

[33] T. Nose, R. Ito, and M. Honma, "Potential of liquid-crystal materials for millimeter-wave application," Appl. Sci., vol.8, no.12, p.2544, 2018.

[34] R. Ito, M. Honma, and T. Nose, "Electrically tunable hydrogen-bonded liquid crystal phase control device," Appl. Sci., vol.8, no.12, p.2478, 2018.

Toshiaki Nose received his B.S. degree in electrical engineering and his M.S. degree in electronic engineering from Tohoku University, Sendai, Japan, in 1983 and 1985, respectively. Since 1985 he had been a Research Associate at Akita University, Akita, Japan and he received ph.D. degree in electronics engineering from Tohoku University in 1995. Since 1999 he has been Professor at Akita Prefectural University, Yurihonjyo, Japan. He has been engaged on research works for liquid crystal optical device applications, and recently it is extended to millimeter-waves and THz waves.

Michinori Honma received master's and doctoral degrees of engineering form Akita University in 1997 and 2000, respectively. Since 2000, he has been engaged in the research on liquid crystal devices in Akita Prefectural University. From April 2000 to September 2004, he was a research associate, and from October 2004, he has been an associate professor. He is a member of the Optical Society, the Institute of Electronics, Information and Communication Engineers, the Japan Society of Applied Physics, the Optical Society of Japan, and the Japanese Liquid Crystal Society. He has been engaged on research works for liquid crystal optical and MMW device applications.

Takashi Sase received his B.E. degree from Akita Prefectural University in 2021. He has been involved in the development of a MMW-SPI system with an LC mask as a student of the master's course at Akita Prefectural University.

Ryota Ito received B.S. degrees of engineering form Akita Prefectural University in 2004. He received M.S. degree in electronic engineering from Tohoku University in 2006. From 2006 to 2012, he was a research associate at Akita Prefectural University. He then obtained his Ph.D. degree in electronics engineering from Osaka University in 2012. Since 2012, he has been an assistant professor at Akita Prefectural University, where he has been engaged in research on THz waves and liquid crystal devices.